



This is a repository copy of *What can be inferred from moiré patterns? A case study of trimesic acid monolayers on graphite.*

White Rose Research Online URL for this paper:

<https://eprints.whiterose.ac.uk/116384/>

Version: Accepted Version

Article:

Spitzer, S., Helmle, O., Ochs, O. et al. (4 more authors) (2017) What can be inferred from moiré patterns? A case study of trimesic acid monolayers on graphite. *Faraday Discussions*, 204. pp. 331-348. ISSN 1359-6640

<https://doi.org/10.1039/C7FD00113D>

Reuse

Items deposited in White Rose Research Online are protected by copyright, with all rights reserved unless indicated otherwise. They may be downloaded and/or printed for private study, or other acts as permitted by national copyright laws. The publisher or other rights holders may allow further reproduction and re-use of the full text version. This is indicated by the licence information on the White Rose Research Online record for the item.

Takedown

If you consider content in White Rose Research Online to be in breach of UK law, please notify us by emailing eprints@whiterose.ac.uk including the URL of the record and the reason for the withdrawal request.



eprints@whiterose.ac.uk
<https://eprints.whiterose.ac.uk/>

What can be inferred from moiré patterns? A case study of trimesic acid monolayers on graphite

Saskia Spitzer,^{a,b} Oliver Helmle,^a Oliver Ochs,^{a,b} Josh Horsley,^c Natalia Martsinovich,^c Wolfgang M. Heckl,^{a,b} and Markus Lackinger^{a,b*}

Received 00th January 20xx,
Accepted 00th January 20xx

DOI: 10.1039/x0xx00000x

www.rsc.org/

Self-assembly of benzene-1,3,5-tricarboxylic acid (trimesic acid - TMA) monolayers at the alkanolic acid-graphite interface is revisited. Even though this archetypal model system for hydrogen bonded porous networks is particularly well studied, the analysis of routinely observed superperiodic contrast modulations known as moiré patterns lags significantly behind. Fundamental questions remain unanswered: Are moiré periodicity and orientation always the same, i.e. is exclusively only one specific moiré pattern observed? What are the geometric relations (superstructure matrices) between moiré, TMA, and graphite lattices? What affects the moiré pattern formation? Is there any influence of solvent, concentration, or thermal treatment? These basic questions are addressed by Scanning Tunneling Microscopy experiments at the liquid-solid interface, revealing a variety of different moiré patterns. Interestingly, TMA and graphite lattices were always found to be $\sim 5^\circ$ rotated with respect to each other. Consequently, the observed variation in moiré patterns is attributed to minute deviations ($< 2^\circ$) from this preferred orientation. Quantitative analysis of moiré periods and orientations facilitates determination of the TMA lattice parameter with picometer precision.

Introduction

Moiré patterns, i.e. the expression of a superperiodicity upon the superposition of two periodic structures, are abundant and can even be observed in daily life. Particularly in surface science, moiré patterns play an important role for epitaxy, when a periodic adsorbate structure grows on a crystalline substrate. True epitaxy implies congruence of adsorbate and substrate lattice at the unit cell level. However, often this strict criterion cannot be met, and one possible alternative is the formation of a higher order superstructure that can be accompanied by a moiré pattern. Experimentally, these moiré patterns can be observed in reciprocal space by low energy electron diffraction (LEED) and other diffraction techniques, or more directly in real space by high resolution scanning tunneling microscopy (STM). Moiré patterns occur in diverse epitaxial system such as sulfur, noble gas or halogen monolayers,¹⁻³ for graphene and hexagonal boron-nitride (h-BN) monolayers on crystalline supports,⁴⁻⁸ but also for self-assembled molecular monolayers.⁹⁻¹² Even the surface of pristine graphite can already show moiré patterns caused by rotational misalignment of the topmost layer.¹³

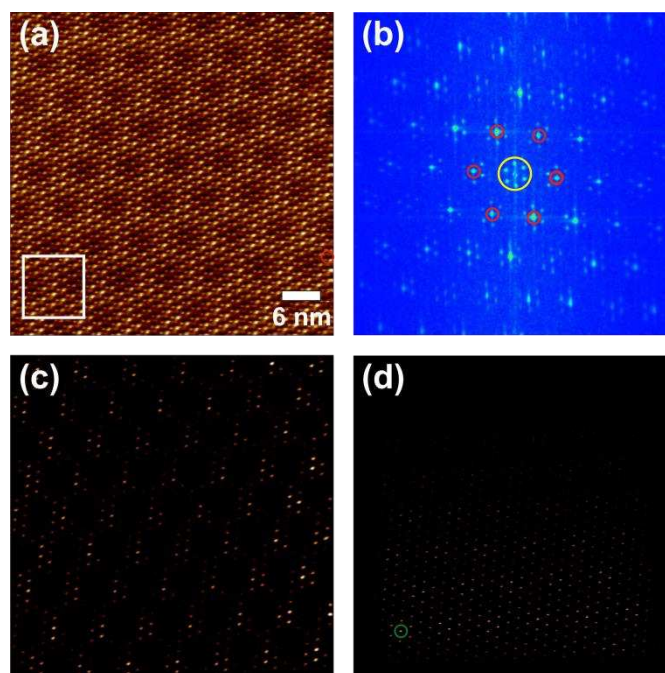


Fig. 1 (a) STM image of the TMA chickenwire structure acquired at the heptanoic acid-graphite(0001) interface (-588 mV, 52 pA) and (b) corresponding FFT (Hannig filter, square root magnitude). First order spots of moiré and TMA are marked by the inner yellow and the outer red circles, respectively (c) Same image as in (a), but low-pass filtered with a cut off just above first order TMA. The colour scale was adjusted to highlight differences between the topographic maxima (d) cross-correlation of the main image (a) with the close-up marked by the rectangle. The green circle indicates the original position of the close-up with the highest intensity.

^a Department of Physics, Technische Universität München, James-Frank-Str. 1, 85748 Garching, Germany; Nanosystems-Initiative-Munich and Center for Nanoscience Schellingstrasse 4, 80799 München, Germany

^b Deutsches Museum, Museumsinsel 1, 80538 München, Germany

^c Department of Chemistry, University of Sheffield, Sheffield S3 7HF, UK

Electronic Supplementary Information (ESI) available: additional STM data and simulation results. See DOI: 10.1039/x0xx00000x

An important distinction of moiré patterns is between commensurate and incommensurate. Commensurate moiré patterns are strictly periodic and originate from the coincidence of adsorbate and substrate lattice at some point. On the other hand, even in the absence of any coincidence incommensurate moiré patterns can emerge. Albeit not strictly periodic, incommensurate moiré patterns exhibit defined spatial beating frequencies. Although this allows definition of a moiré lattice, the corresponding unit cells are not equivalent. Graphene grown by chemical vapour deposition on transition metal surfaces is a versatile example, where both types of moiré patterns are observed, for instance incommensurate on Cu(111)⁸ and commensurate on Ru(0001).⁴ Especially for very large moiré unit cells, the experimental distinction between commensurate and incommensurate moirés can become challenging, if not impossible. More complex epitaxial systems can also show a combination with commensurate domains separated by incommensurate soliton walls.^{7, 14}

Commensurate moiré patterns can be viewed as actual superstructures and accordingly be described by a unit cell and a lattice defined through base translation vectors $\vec{A}_{\text{moiré}}$ and $\vec{B}_{\text{moiré}}$. These are simultaneously lattice vectors of both adsorbate and substrate lattice:

$$\vec{A}_{\text{moiré}} = a_{11} \cdot \vec{a}_{\text{surf}} + a_{12} \cdot \vec{b}_{\text{surf}} \quad (1)$$

$$\vec{B}_{\text{moiré}} = a_{21} \cdot \vec{a}_{\text{surf}} + a_{22} \cdot \vec{b}_{\text{surf}} \quad (2)$$

as well as:

$$\vec{A}_{\text{moiré}} = b_{11} \cdot \vec{a}_{\text{ads}} + b_{12} \cdot \vec{b}_{\text{ads}} \quad (3)$$

$$\vec{B}_{\text{moiré}} = b_{21} \cdot \vec{a}_{\text{ads}} + b_{22} \cdot \vec{b}_{\text{ads}} \quad (4)$$

with integer coefficients a_{ij} and b_{ij} , respectively; \vec{a}_{surf} , \vec{b}_{surf} and \vec{a}_{ads} , \vec{b}_{ads} denote the base translation vectors of surface and adsorbate lattice, respectively. Conversely, if $\vec{A}_{\text{moiré}}$ and $\vec{B}_{\text{moiré}}$ are lattice vectors of adsorbate or substrate lattice, the reciprocal lattice vectors of adsorbate or substrate are lattice vectors of the reciprocal moiré lattice.

Moiré patterns were subject of many experimental and theoretical studies over the last decades, and their emergence in the context of graphene and other 2D materials has led to a renaissance. An interesting, but understudied model system for moiré patterns are self-assembled molecular monolayers on crystalline surfaces. The present contribution focusses on weakly interacting graphite surfaces, where moiré patterns are more commonly observed than on metal surfaces. In addition, straightforward experiments can be carried out at liquid-solid interfaces: Molecules are dissolved in appropriate dielectric solvents (e.g. phenyloctane, 1,2,4-trichlorobenzene, alkanolic acids, etc.) and the solution is then applied to inert substrates, mostly graphite. In most cases, STM is used for characterization in facile experiments, where the tip is directly immersed into solution.¹⁵⁻¹⁸

However, moiré patterns are more than just a peculiar phenomenon, and profound insights can be obtained from

their detailed analysis. As a result of the subtle balance between molecule-molecule and molecule-surface interactions, moiré patterns can provide evidence on the relative strength of intermolecular and surface potential. Moreover, the moiré structure parameters can be utilized to determine adsorbate lattice parameters with unprecedented precision, exceeding that of standard STM measurements by orders of magnitude.^{12, 19} These precise and reliable data can serve as pivotal benchmark for structure simulations.

The moiré patterns of molecular adlayers exhibit important differences in comparison to graphene or h-BN: lattice parameter differences between molecular adlayers and surface are typically large, whereas graphene ($a_{\text{graphene}} = 0.246 \text{ nm}$) and its supports feature almost similar lattice parameters (e.g. $a_{\text{Ir}(111)} = 0.271 \text{ nm}$). Molecular adlayers are stabilized by relatively weak non-covalent intermolecular bonds such as hydrogen or van der Waals bonds. Consequently, molecular lattices are more flexible and adaptive as compared to the covalently interlinked counterparts. Lastly, graphene and h-BN are grown at high temperatures typically up to 1000 °C, and in most cases studied at room temperature or even below after cooling down. Owing to differences in the thermal expansion between graphene and underlying metal surface, the lattice parameters ratios at growth vs. characterization temperature can differ, with implications for the moiré. In contrast, the molecular monolayers at the liquid-solid interface are normally studied at room temperature, i.e. the same temperature where they self-assembled.

In the following, the routinely observed moiré patterns in hydrogen bonded monolayers of benzene-1,3,5-tricarboxylic acid (trimesic acid - TMA) on graphite are analysed and discussed in more detail.

Results and Discussion

TMA on graphite was chosen as a model system for this study, because it reliably self-assembles into long-range ordered structures with clearly discernible moiré pattern in STM. Despite its simple chemical structure, rigidity, and high symmetry, self-assembly of TMA is complex and shows rich behaviour with different surface polymorphs.²⁰⁻²⁸ Yet, the so called chickenwire structure – a hexagonal porous honeycomb network with a lattice parameter of $\sim 1.7 \text{ nm}$ and a pore diameter of $\sim 1.0 \text{ nm}$ – is the most abundant structure (cf. inset in Fig. 5). Other, typically more densely packed polymorphs were observed for various conditions and preparation procedures. For instance, at the liquid-solid interface TMA self-assembly is known for solvent-induced polymorphism, where a polymorph called flower structure occurred with shorter chain length alkanolic acids as solvents.²⁸ The chickenwire polymorph exclusively features two-fold cyclic $R_2^2(8)$ hydrogen bonds in a straight geometry between all carboxylic acid groups of each TMA. Owing to the high bond strength of these resonance enhanced hydrogen bonds,²⁹ the network is also relatively strong: for a free-standing TMA monolayer a binding energy of 1.28 eV per molecule (corresponding to 0.86 eV per double

hydrogen bond) is obtained from dispersion-corrected density functional theory (DFT) simulations. In addition, TMA molecules also adsorb strongly on graphite with an adsorption energy of ~ 0.86 eV for isolated molecules according to molecular mechanics simulations. Both contributions total in an overall binding energy in excess of ~ 2 eV per TMA molecule in the adsorbed monolayer. Interestingly, in accord with a previous study,²⁵ the TMA adsorption energy on graphite did not vary significantly between different sites, indicating a shallow surface potential.

Over the years TMA has become a fairly well-studied model system. Yet, its moiré patterns were not analysed in greater detail. Fig. 1 shows a large scale STM image of the self-assembled TMA chickenwire structure at the heptanoic acid-graphite interface. The apparent height of the honeycomb network is periodically modulated with hexagonal symmetry. The structural origin of this moiré pattern lies in the mismatch between TMA and underlying graphite lattice. The moiré pattern is also clearly recognizable in reciprocal space as illustrated by the corresponding two-dimensional Fast Fourier Transform (FFT) in Fig. 1(b). First order TMA spots are marked by the red circles, and higher orders exhibit significant intensity. The larger spatial periodicity of the moiré gives rise to the inner Fourier components marked by the yellow circle. The hexagonally arranged satellites around TMA spots are a further manifestation of the moiré.

Emergence of a moiré with large period clearly indicates incommensurability of TMA and graphite at the level of a single or a few unit cells. This implies that TMA dimers – the basic structural motif – are not adsorbed on equivalent sites. As a further consequence, the pores defined by six surrounding TMA molecules feature different positions with respect to graphite with important implications for host-guest chemistry. An illustrative example, therefore, are coronene (COR) guest molecules. Their snug fit in the TMA pores prohibits any lateral degrees of freedom, hence the COR adsorption sites are rigorously defined by the TMA lattice.³⁰ In STM images the spatial variation of adsorption sites within the pores manifest themselves as pronounced intramolecular contrast modulation of COR guests.³¹

Although the TMA moiré on graphite was already reported some time ago,³² a detailed analysis is still outstanding. Even the fundamental question of commensurability has not been addressed so far? A possible first step is expressing $\vec{A}_{\text{moiré}}$ as linear combination of \vec{a}_{ads} and \vec{b}_{ads} . In principle, this could be done simply by counting in the STM images. However, one may encounter ambiguities, so a reciprocal space analysis provides spatially averaged, and hence potentially more accurate information. According to crystallographic notation, base translation vectors with 120° angle are used for all hexagonal lattices in the following. The subsequent analysis is exemplified for hexagonal lattices, but could similarly be adapted to other lattices. A practical way to find the coefficients b_{ij} of equation (3) and (4) is to first determine the

length ratio of the lattice vectors Φ by direct measurement in the FFT:

$$\Phi = \frac{|\vec{A}_{\text{moiré}}^*|}{|\vec{a}_{\text{ads}}^*|} = \frac{|\vec{a}_{\text{ads}}^*|}{|\vec{A}_{\text{moiré}}^*|} \quad (5)$$

Asterisks denote reciprocal lattice vectors. Similarly the rotation angle α (defined as the smallest angle between \vec{A}_{ads}^* and $\vec{A}_{\text{moiré}}^*$) can be directly inferred from the FFT. Then the coefficients can be determined according to:

$$b_{11} = \Phi \cdot (\cos \alpha + \frac{1}{\sqrt{3}} \cdot \sin \alpha) \quad (6)$$

$$b_{12} = \frac{2}{\sqrt{3}} \cdot \Phi \cdot \sin \alpha \quad (7)$$

$$b_{21} = -b_{12} \quad (8)$$

$$b_{22} = b_{11} - b_{12} \quad (9)$$

Unless all coefficients are integers, the moiré is incommensurate. However, how large are the acceptable tolerances for these experimental values? STM imaging, and even more so experiments under ambient conditions, are prone to image distortions caused by thermal drift as well as piezo creep and hysteresis. Consequently, “real space crystallography” requires as undistorted as possible images. In any case, the coefficients should be evaluated for subsequent up and down scans to judge the reproducibility. Further inaccuracies can result from the width of the FFT peaks that is inversely proportional to the number of periods. Hence it is important that the STM images capture a sufficient number of moiré periods, while the pixel resolution of the molecular lattice should be high enough to avoid aliasing effects. This condition becomes increasingly intricate to fulfil with increasing moiré period.

Applying this procedure to the image in Fig. 1(a) results in $b_{11} = 4.77 \pm 0.06$ (4.78 ± 0.04) and $b_{12} = 1.64 \pm 0.06$ (1.65 ± 0.06), clearly indicating incommensurability.⁵ Values in parentheses refer to the subsequently acquired down scan, indicating a quite satisfying reproducibility, even though some residual drift remained during STM imaging. Comparing two lattices in the same image means that any possible distortion similarly affects both lattices, resulting in beneficial error compensation. So it is less surprising that determination of the coefficients from a distortion-corrected image with enforced hexagonal TMA lattice resulted in similar coefficients.

The non-integer coefficients indicate incommensurability of the moiré with respect to the TMA lattice. This not necessarily, but reasonably also implies incommensurability of TMA and graphite lattice. In theory, true incommensurability requires irrational coefficients, because any rational coefficients have integer multiples. Nevertheless, we conclude practical incommensurability of the TMA lattice for the following reason: even under favourable assumptions, i.e.

$$b_{11} = 4\frac{3}{4} \text{ and } b_{12} = 1\frac{2}{3}$$

commensurability is only achieved after 12 moiré periods, a length that possibly exceeds the domain size. More importantly, a pronounced and specific energetic preference for such exceedingly large unit cells appears highly unlikely. So this lattice relation is presumably not related to the presence of few energetically favourable adsorbate positions on the surface.

Concluding incommensurability also means that the moiré unit cell is not an actual repeat unit. Even though this should be directly visible in the STM image, it is relatively difficult to recognize. Hence the STM image in Fig. 1(a) was further processed by low-pass filtering in Fourier space with a cut off frequency just above first order TMA. The so processed image is shown in Fig. 1(c) with adjusted colour scale to highlight the topographic maxima. While largely arranged on the moiré lattice, these groups of maxima appear clearly different at different moiré lattice points. This violation of translation symmetry further confirms the incommensurability of the TMA moiré on graphite. This is further substantiated by the cross-correlation shown in Fig. 1(d), evaluated for the close-up marked in Fig. 1(a) with its main image. This cross-correlation shows maxima with a distribution corresponding to the TMA lattice, because relative shifts with the TMA periodicity result in a certain level of coincidence. However, slightly higher intensities result for the simultaneous coincidence of both TMA and moiré lattice. Accordingly, for a fully commensurate moiré equally strong intensity maxima should appear with the moiré periodicity. This is clearly not the case in Fig. 1(d), where the colour scale was adjusted to highlight differences across the cross-correlation. Some higher intensities, i.e. more favourable coincidences, are still observed in the vicinity of the original position of the close-up, yet the intensities decay for increasing distance. This indicates dephasing of TMA and moiré for increasing distance, and hence incommensurability. For further illustration, the same image processing procedures were applied to simulated commensurate vs. incommensurate moiré patterns (cf. ESI).

Kinetics vs. thermodynamics

The unexpected incommensurability also gives rise to the question whether the experimentally observed structure is thermodynamically most stable or whether it is a metastable intermediate. Intuitively, one would expect a higher order commensurate structure as energetic optimum. The intermolecular arrangement of TMA in the chickenwire polymorph exhibits only energetically ideal hydrogen bonds, hence it is the energetically most stable structure per molecule. However, as recently worked out, the free energy per unit area is decisive for the relative thermodynamic stability of competing structures.³³ This might also lead to a thermodynamic preference for polymorphs with energetically inferior intermolecular bonds, but higher packing density.³⁴ Furthermore, the thermodynamically most stable structure is

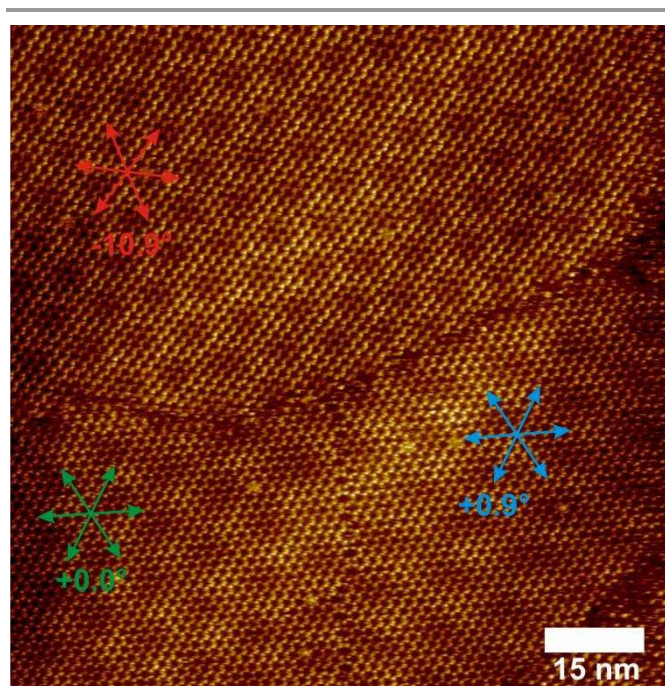


Fig. 2 Overview STM image of the TMA chickenwire structure obtained at the heptanoic acid-graphite interface (-500 mV, 40 pA). Each of the three larger domains shows an individual moiré pattern with different period and orientation. The orientation of the TMA lattice in the green marked domain in the lower left corner was defined as 0°, the other angles are stated relative to this reference. Arrows indicate equivalent directions of the TMA lattices.

not only defined by the intermolecular arrangement, but also by its epitaxy with respect to the underlying surface. Here optimization of molecule-surface interactions should be most important, with only minor influences of entropy variations. In other terms, the thermodynamically most stable adsorbed TMA monolayer structure is also characterized by a unique epitaxial relation with respect to graphite. Accordingly, in thermodynamic equilibrium either no moiré or exclusively one distinct moiré should be observed. Again a comparison to covalently linked networks, i.e. graphene epitaxially grown on transition metal surfaces, is instructive: on Ir(111) different moiré patterns with 0°, 14°, 18.5°, and 30° orientation are observed,^{5, 35} whereas on Rh(111) only one distinct moiré pattern is known.³⁶ Moreover, on Ir(111) growth temperature and rate influence the graphene moiré patterns, indicating the importance of nucleation and growth kinetics even for networks that feature the ultimate bond strength.

The large scale STM image obtained in heptanoic acid in Fig. 2 shows three domains with moiré patterns, but each with a different period and orientation. Interestingly, an earlier study reported just one distinct moiré for the TMA network itself, and another one for the TMA network with incorporated COR guest molecules.³² With reference to the discussion above, our experimental finding provides evidence for a kinetically controlled and trapped system. Although self-assembly favours the chickenwire polymorph, the molecule-surface interactions do not attain the energetic optimum.

Closer inspection of relative domain orientations provides further information. While the orientations of the lower left and right domain differ by only 0.9° , the upper domain has a relative orientation of $\sim 11^\circ$. In all STM data either more or less aligned or $\sim 10^\circ$ rotated domains were consistently observed, suggesting a relative rotation between TMA and graphite lattice of approximately $\pm 5^\circ$. This finding is further corroborated by split-images (vide infra, ESI), and in accord with an earlier study³² as well as recent work by the groups of Rosei and De Feyter.²⁵ The invariant rotational orientation of TMA with respect to graphite in combination with the fact that moiré parameters respond extremely sensitive to rotation angle changes,³⁷ suggest that minute deviations from this preferred rotational orientation account for the variety of experimentally observed moirés.

Solvent dependence and heating experiments

Similar observations, i.e. various different moiré patterns, either $\sim 0^\circ$ or $\sim 10^\circ$ relative domain orientations, and $\pm 5^\circ$ orientation between TMA and graphite, were also made with nonanoic acid as solvent, suggesting no or a very minor solvent influence.

The general reason for kinetic trapping is insufficient thermal energy to overcome barriers. Consequently, a transition into a thermodynamically more stable or most stable state could be promoted by heating. Since these transitions are irreversible, characterization at elevated temperatures is not required, and ex-situ studies after cooling down to room temperature are sufficient. However, care has to be taken because of unwanted chemical reactions between solute and solvent. Heating TMA in nonanoic acid solution to only $\sim 50^\circ\text{C}$ already results in intense yellow discolouration, indicating chemical changes of TMA, most probably anhydride formation with solvent molecules. This also affects TMA self-assembly, where an overall chickenwire structure is still observed, but with many defects. While these experiments with defective TMA molecules can provide further insights into dynamic exchange and self-healing properties, extensive heating experiments to promote thermodynamical equilibration are ruled out for TMA with alkanic acids. Improvements for homologous alkanic acid solvents or lower concentrations cannot be expected. In principle, adding water should shift the equilibrium for the reversible anhydride formation, but might also induce competitive hydrogen bonding. Carrying out experiments without solvent under ultra-high vacuum (UHV) conditions would be a feasible alternative, but this sacrifices the possibility to study the important role of dynamic exchange with solution for equilibration.

Nevertheless, heating experiments in solution were performed in a slightly different manner: First the pristine graphite sample (without any solution applied) was heated up to $\sim 100^\circ\text{C}$ on a hot plate. Then the graphite was removed from the hot plate and room temperature solution was immediately applied to the hot surface. The sample was allowed to cool down to

room temperature and subsequently characterized by STM. This type of experiments offers less control than a slow heating experiment, because the exact temperature profile during cooling depends on heat capacities and transport. However, this approach facilitates self-assembly studies at relatively high temperatures, while minimizing the risk of chemical alterations. Longer exposure times are still not possible, but according to the Arrhenius law the influence of temperature is significantly more severe than that of time. For the proposed experiments, at least TMA self-assembly takes place at elevated temperatures with increased chances to avoid kinetic trapping. Subsequently acquired STM images show the chickenwire polymorph without any defects. The still present moiré patterns were likewise incommensurate and similar to those observed for room temperature samples. Only a not further studied increase in domain size was observed, indicating thermal activation of Ostwald ripening.

Reciprocal space analysis

The period of commensurate moiré patterns is unambiguously defined by the smallest translation between two coincidence points of adsorbate and substrate lattice. Once the (integer) coefficients of the moiré lattice vectors with respect to adlayer and surface are known, the adsorbate lattice parameter can be determined with the precision of the surface lattice parameters. An intriguing question is, whether the incommensurate moiré patterns of TMA on graphite can similarly be utilized to precisely determine adsorbate lattice parameters. For incommensurate moiré patterns it is less obvious, how the moiré parameters are related to the relative rotation and lattice parameters of adsorbate and surface. Recently Günther et al. reported an intuitively understandable method for the geometric construction of moiré beating frequencies.³⁷ Their approach aimed to explain the multitude of moiré patterns observed for graphene on transition metal surfaces. Therefore it was exemplified for hexagonal lattices with comparable lattice parameters, but is generally applicable. In analogy to optics, the moiré was obtained as product of two lattice-periodic functions, representing adlayer and surface, respectively:

$$f_{\text{moiré}}(x, y) = f_1(x, y) \times f_2(x, y) \quad (10)$$

According to the convolution theorem, the Fourier transform of the moiré $\mathcal{F}\{f_{\text{moiré}}\}$ is equal to the convolution of the Fourier transforms of f_1 and f_2 :

$$\mathcal{F}\{f_{\text{moiré}}\} = \mathcal{F}\{f_1\} \otimes \mathcal{F}\{f_2\} \quad (11)$$

In $\mathcal{F}\{f_{\text{moiré}}\}$ additional Fourier components with sizable intensities occur for connecting vectors between strong Fourier components in $\mathcal{F}\{f_1\}$ and $\mathcal{F}\{f_2\}$. Orientation and period of the moiré lattice are defined by the shortest of these vectors.

In the following, this approach is applied to TMA monolayers on graphite, whose reciprocal lattices are both hexagonal and 30° rotated with respect to the corresponding real space lattices. In order to draw both TMA and graphite reciprocal

lattices together, the ratio of the real space lattice parameters and relative rotation angle are required. This information can best be obtained from STM in so called “split-images”, where the tunnelling parameters are changed to subsequently image adsorbate and substrate within the same scan frame. From split-images a rotation angle of $\alpha = 5^\circ$ and a TMA-to-graphite lattice parameter ratio of ~ 6.75 can be acquired, corresponding to $a_{TMA} = 1.66 \text{ nm}$. Interestingly, the rotation angles in all split-images agreed within $\pm 1^\circ$ (ESI), in accord with the observed relative domain orientations as discussed above as well as literature.^{25, 32} This experimental TMA lattice

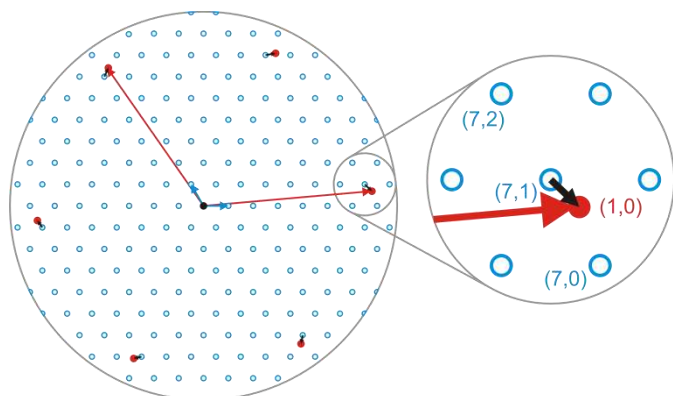


Fig. 3 Reciprocal lattices of TMA (blue open circles) and graphite (red closed circles) drawn for a relative rotation of $\alpha = 5^\circ$ and $a_{TMA} = 1.66 \text{ nm}$. Red and blue arrows indicate the base translation vectors of the respective reciprocal lattices. The close-up on the right hand side shows the vicinity of the (7,1) TMA Fourier component which is closest to the (1,0) graphite Fourier component. The black rather short arrows indicate the resulting base translation vectors of the moiré reciprocal lattice.

parameter also agrees well with our own and previously published DFT simulations.^{25, 32}

Fig. 3 shows a sketch of both TMA and graphite reciprocal lattices according to the experimental data. The closest proximity between lattice points of both reciprocal lattices occurs between (7,1) TMA and (1,0) graphite. This finding already highlights an important difference to graphene on transition metals: both have comparable lattice parameters, so the closest proximity appears between Fourier components of comparable order, e.g. (2,0) and (1,1). Owing to the almost seven-fold difference in lattice parameter between TMA and graphite, this is simply not possible, and inevitably requires involvement of higher order TMA Fourier components. In contrast, a contribution from higher order graphite Fourier components (e.g. (2,0) graphite) appears rather unlikely, because the intensity of the required TMA Fourier components at $\sim 14^{\text{th}}$ order is extremely low. Otherwise higher order moiré Fourier components should also be experimentally observed which is not the case. According to this geometric construction, the base translation vector of the reciprocal moiré lattice $\vec{A}_{\text{moiré}}^*$ (short black arrow in Fig. 3) is given by:

$$\vec{A}_{\text{moiré}}^* = (1 \cdot \vec{a}_{\text{graphite}}^* + 0 \cdot \vec{b}_{\text{graphite}}^*) - (7 \cdot \vec{a}_{TMA}^* + 1 \cdot \vec{b}_{TMA}^*) \quad (12)$$

From here the moiré period can be calculated as a function of the rotation angle α between TMA and graphite lattice using simple trigonometry. The results are shown in Fig. 4 for rotation angles in the vicinity of the experimental value $\alpha = 5^\circ$ and for three slightly different TMA lattice parameters around the experimental value. In all cases, the largest moiré lattice parameter is obtained for $\alpha \approx 7.6^\circ$, i.e. when the (1,0) graphite and (7,1) TMA reciprocal lattice vectors are aligned, resulting in the shortest $\vec{A}_{\text{moiré}}^*$. The moiré period also increases with decreasing a_{TMA} , because the corresponding enlargement of a_{TMA}^* further decreases the length of $\vec{A}_{\text{moiré}}^*$ as evident from Fig. 3. It is worth noting that this plot is only valid

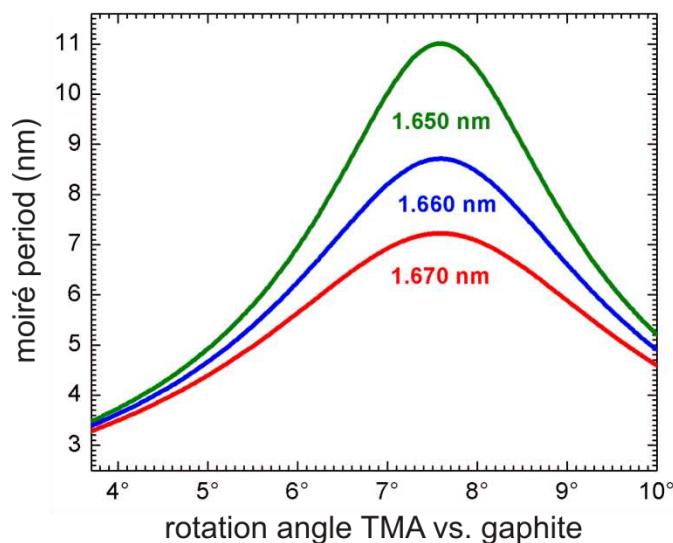


Fig. 4 Moiré period as a function of relative rotation between TMA and graphite lattices around the experimental value $\alpha = 5^\circ$. The plot assumes the closest proximity between (1,0) graphite and (7,1) TMA Fourier components, respectively. The moiré period also depends on the TMA lattice parameter as illustrated by the different curves for specific a_{TMA} as indicated.

for $3.7^\circ < \alpha < 11.7^\circ$. Outside this range the distance between (1,0) graphite and (7,0) or (7,2) TMA becomes shorter than to (7,1) TMA, and hence defines $\vec{A}_{\text{moiré}}^*$.

The graphs in Fig. 4 demonstrate how slight variations of α result in large variations of moiré period $A_{\text{moiré}}$. However, the same is true for modest variations of a_{TMA} . For instance, for fixed $\alpha = 6^\circ$, $a_{TMA} = 1.650 \text{ nm}$ results in $A_{\text{moiré}} = 6.9 \text{ nm}$, whereas $a_{TMA} = 1.670 \text{ nm}$ results in a notably smaller value of $A_{\text{moiré}} = 5.6 \text{ nm}$.

In order to judge the adaptability of the TMA lattice, DFT calculations of the energy vs. a_{TMA} were performed. The results shown in Fig. 5 indicate a relatively shallow energy minimum at $a_{TMA} = (1.650..1.660) \text{ nm}$, allowing slight variations of TMA lattice parameters at modest energy costs.

Since the moiré period is sensitive to both α and a_{TMA} , the origin of the variety of moiré patterns is not a priori clear. Yet, again images at domain boundaries provide further insights. The two lower domains in Fig. 2 show only a small, but detectable relative rotation of $\sim 1^\circ$, but different moiré patterns, suggesting a major influence of α .

So far only moiré periods were analysed. Yet, even overview STM images provide further easily accessible information, namely the rotation angle φ between moiré and TMA lattice. Theoretical values for φ can similarly be derived from the geometrical construction in Fig. 3 as a function of α with a_{TMA} as additional parameter (cf. ESI). For further analysis, however, a combined plot of moiré orientation vs. periodicity as shown in Fig. 6 is more useful. Constant values of a_{TMA} result in iso-lines that uniquely correlate moiré orientation and period. This diagram highlights once more the extreme sensitivity of both moiré period and orientation to slight variations in a_{TMA} . For

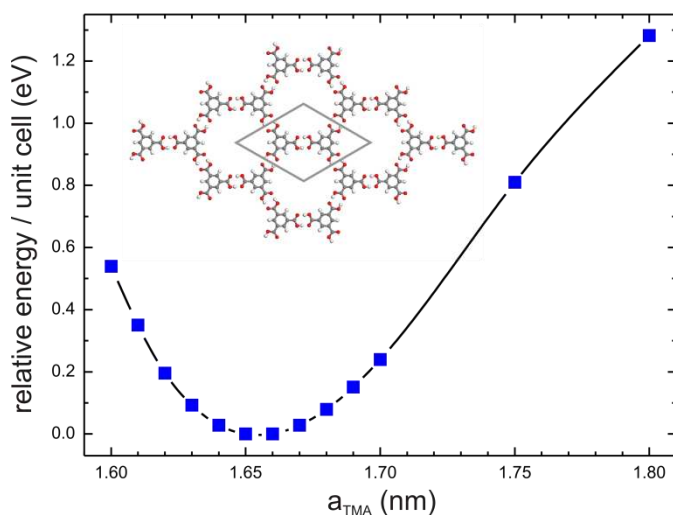


Fig. 5 DFT-derived energies per unit cell for a free-standing TMA honeycomb network (i.e. surface neglected) as a function of the lattice parameter of a hexagonal lattice. The black line serves a guide to the eye. The curve shows a relatively shallow minimum at 1.650 nm .. 1.660 nm. The inset depicts the optimized structure (unit cell marked, grey: carbon; red: oxygen, white: hydrogen)

further analysis, experimentally observed moiré patterns (cf. ESI) were evaluated in large scale STM images[‡] and included in the diagram in Fig. 6 as one data point for each observed moiré.

Despite the fact that data were acquired with different solvents (heptanoic vs. nonanoic acid) and for different preparation protocols (deposition onto room temperature vs. heated surfaces) all data points fall onto the same iso-line, (thicker grey line) corresponding to $a_{TMA} = (1.652 \pm 0.002)nm$. Moreover, the literature value from ref. 32 (blue full circle) also falls on the same iso-line. Based on the small deviations, we propose that the comparison of easily and reliably measurable moiré parameters to the reciprocal space model facilitates the determination of a_{TMA} with picometer precision.

Materials and Methods

STM data were acquired at the solid-liquid interface using home-built instruments driven by an ASC 500 and SPM 100 control electronics from attocube systems AG and RHK, respectively. All voltages refer to the sample. A droplet of TMA

in heptanoic or nonanoic acid solution was applied to the freshly cleaved surface of highly oriented pyrolytic graphite. Images were recorded with mechanically cut PtIr tips directly immersed into solution. For any measurement, the instruments were allowed to equilibrate until the similarity of subsequent up and down scans indicated low drift.

DFT calculations were performed for free-standing TMA monolayers with the CP2K software³⁸ using the PBE functional³⁹ and empirical dispersion correction.⁴⁰ DZVP basis sets were used for all atoms. Periodic boundary conditions were applied, using a hexagonal unit cell with variable $a = b$ and fixed $c = 1.00 nm$. No further constraints were applied.

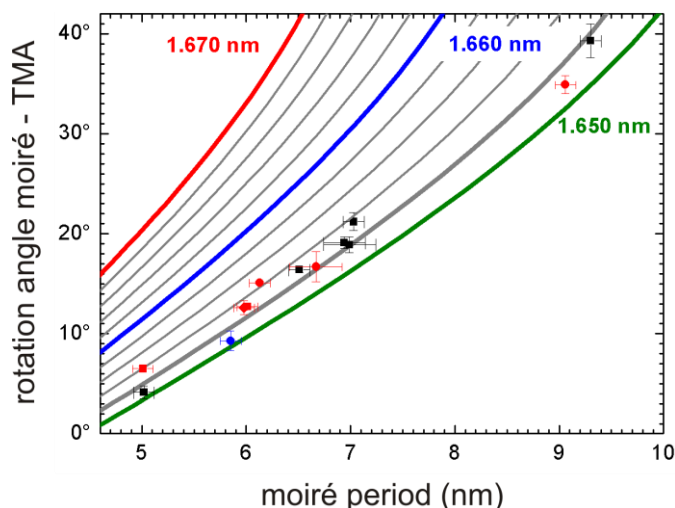


Fig. 6 Theoretical curves for the moiré orientation with respect to graphite vs. the moiré period. The curves were evaluated for different a_{TMA} as indicated. Along each curve the rotation angle α between TMA and graphite lattice varies (approximately from 4° to 8°). The gray lines represent iso-lines for increments of $\Delta a_{TMA} = 0.002 nm$. Each data point corresponds to one moiré pattern observed in an independent experimental run in heptanoic acid (black squares) or nonanoic acid (red circles: room temperature deposition, red squares: deposition onto hot surface, red diamond: image acquired at 50 °C after room temperature deposition) (cf ESI) The blue circle represents a literature result.³²

Summary and Conclusions

In summary, the moiré patterns routinely observed for the TMA chickenwire polymorph on graphite were studied in greater detail. The precise evaluation of the moiré lattice parameters with respect to the TMA lattice reveals incommensurability of both lattices. This is further corroborated by the observed aperiodicity in the STM images, related to the dissimilarity of the moiré unit cells. This surprising finding indicates a weak preference of TMA-graphite interactions for specific sites (i.e. modest spatial variation of the surface potential) as compared to the strong intermolecular TMA-TMA hydrogen bonds.

Moreover, various moiré patterns with different period and orientation were found. This indicates that the samples are not in thermodynamical equilibrium, but are kinetically stabilized. Yet it was not possible to influence the moiré pattern

formation by providing thermal energy in experiments with deposition of solution onto heated surfaces.

However, the TMA lattice is not statistically oriented with respect to graphite, but was always found with a relative rotation of $\sim 5^\circ$. This was inferred either directly from split-images or indirectly from the $\sim 10^\circ$ angle found between differently oriented TMA domains. Consequently, the variety of different moiré patterns is explained by slight deviations from this preferred orientation. The non-random orientation between TMA and graphite lattice implies that the reciprocal moiré lattice vector always occurs between the same Fourier components, i.e. (7,1) TMA and (1,0) graphite. This provides the basis for a quantitative analysis, where both moiré period and orientation are expressed as functions of the TMA-graphite rotation angle α . In addition, the moiré parameters sensitively depend on the exact value of the TMA lattice parameter, where even picometer changes in a_{TMA} having a notable effect on $A_{moiré}$. Accordingly, the TMA lattice parameter can be derived from moiré period and orientation, quantities that are both easily and accurately accessible from STM data. Interestingly, for all moiré patterns observed irrespective of solvent or heat treatment a TMA lattice parameter of $a_{TMA} = (1.652 \pm 0.002)nm$ is obtained. This not only suggests picometer accuracy, but also corroborates a quite rigid nature of the TMA lattice, also in the presence of an evidently weak surface potential.

A clear advantage of this approach is that the input data, i.e. moiré period and orientation, can be measured in relatively large scale STM images in the order of 50 - 100 nm, where drift is less of a problem than for atomically resolved images. Moreover, image distortions simultaneously affect both moiré and TMA lattice, thus errors partly compensate. The preferred rotational alignment of TMA with respect to graphite of $\sim 5^\circ$ is convenient, as it implies that always the same Fourier components are involved in the moiré formation. If this would not be the case, knowledge of the adsorbate-substrate rotation angle would be required for each recorded moiré. Yet, approximate values for α with STM accuracy are sufficient in order to determine the involved Fourier components. In practice, a split-image has to be acquired along with each moiré.

Finding an incommensurate moiré for TMA on graphite leads to many further interesting research questions: What drives the preferred orientation of TMA with respect to graphite? What controls the formation of incommensurate domains and what stabilizes them? Finally, what is the thermodynamically most favourable structure of TMA on graphite?

As for the stabilization, the absence of Ostwald ripening in TMA monolayers at room temperature, i.e. the coalescence of domains in order to minimize energetically unfavourable domain boundaries, plays an important role. At room temperature, coalescence is only observed for comparatively small TMA domains, whereas larger domains remain stable.⁴¹

Most domain boundaries are straight and exhibit defined crystallographic orientations, i.e. $\langle 10 \rangle$ or $\langle 12 \rangle$ with respect to the TMA lattice. This implies that TMA molecules at domain boundaries are still hydrogen bonded to two adjacent TMA molecules, and consequently stabilized by two pairs of resonance enhanced cyclic hydrogen bonds. According to Molecular Mechanics simulations,⁴¹ this gives rise to a high binding energy of 1.81 eV per TMA molecule, explaining the high stability and persistence of domain boundaries.⁴¹

A further interesting observation – in particular for an incommensurate structure – is the preferred rotational orientation of $\sim 5^\circ$ with respect to graphite. Most likely, this orientation preference is already predetermined at an early stage of growth, since a concerted reorientation of domains will most likely not take place beyond a certain size. In this respect, a small size of the critical nucleus for TMA monolayers can be presumed. Accordingly, the growing TMA domains become thermodynamically stable at a relatively small size, i.e. the preferred orientation of a few TMA molecules – maybe as little as two – with respect to graphite, already determines the domain orientation that is then kinetically trapped. Of course, this does not yet explain the energetic preference for this specific orientation. Relating to this, an important contribution might arise from the preference of more strongly interacting oxygen atoms for specific sites.⁴² In any case, farther-reaching quantum chemical simulations of TMA on graphite are likely to aid in elucidating the prominent preference for the $\sim 5^\circ$ orientation. In this respect, it might be necessary to consider at least TMA dimers, i.e. the two non-equivalent molecules within the unit cell, or even larger aggregates as cyclic hexamers rather than just individual TMA molecules. Further insights could be expected from a full evaluation of the adsorption energy as a function of rotational orientation of TMA with respect to graphite. A relatively shallow energy minimum could explain the small orientational deviations that eventually account for the variety of observed moiré patterns.

Finding an incommensurate moiré for TMA on graphite is still a surprising result. One would expect that reasonably strong spatial variations of TMA-graphite interactions should result in preferred adsorption sites and orientations, and hence promote commensurability. This may not be achievable at the level of a single unit cell, but doubling or tripling the unit cell already increases the number of possibilities of favourable adsorption sites substantially. Thereby the almost seven-fold difference between TMA and graphite lattice parameters fosters a large number of possibilities. Moreover, the relatively small strain energy of the chickenwire structure (cf. Fig. 5) implies some adaptability of the TMA lattice parameter. Both factors should promote the lock-in into a high order commensurate structure. On the other hand, it can be shown that for a sufficiently small corrugation of the surface potential incommensurate superstructures can become energetically favourable.¹⁴ In this respect, evaluation of monolayer energies in reciprocal space based on the Fourier components of the surface potential as previously proposed for commensurate

superstructures,⁴³ is a very promising approach. Without any doubt, the situation with reduced-symmetry adsorbates as the molecules requires adaptations and can become quite challenging, but avoids the notorious problems with applying periodic boundary conditions to incommensurate structures.

Our comparative experiments in heptanoic vs. nonanoic acid suggest a negligible solvent influence on both the preferred rotational orientation and the precise TMA lattice parameter. In this regard further studies in the absence of solvent, i.e. under UHV conditions might be interesting. While the nucleation kinetics at the liquid-solid interface is determined by adsorption rates that cannot be directly controlled, the deposition rate in UHV is an experimental parameter, and typically many orders of magnitude lower. Moreover, growth of TMA domains could also be studied at lower temperature with reduced influence of thermal fluctuations.

In summary, we have demonstrated a straightforward method to extract precise values for lattice parameters of adsorbed molecular monolayers from the analysis of incommensurate moiré patterns as routinely observed for TMA monolayers on graphite. In this respect, it would be interesting to apply this method to comparable systems in order to see whether a similar level of precision is attainable.

Acknowledgements

O.O. gratefully acknowledges generous financial support by the Helmut-Fischer-Stiftung. J.H. and N.M. acknowledge the access to the high-performance computing cluster Iceberg at the University of Sheffield.

Notes and references

[§] length and angles were measured in the FFTs and averaged over the three symmetrically equivalent directions. Maximum deviations are stated as errors.

[‡] these values were obtained from distortion-corrected images with hexagonal TMA layers and averaged over symmetrically equivalent pairs of Fourier components. Maximum deviations are stated as errors.

[†] This binding energy also includes molecule-surface interactions and was obtained using the standard Dreiding force field that features an explicit hydrogen bonding term, but does not account for the resonance enhancement of two-fold cyclic hydrogen bonds.

- 1 D. Wang, Q. M. Xu, L. J. Wan, C. Wang and C. L. Bai, *Surf. Sci.*, 2002, **499**, L159-L163.
- 2 N. S. Komarov, T. V. Pavlova and B. V. Andryushechkin, *Surf. Sci.*, 2016, **651**, 112-119.
- 3 F. Brunet, R. Schaub, S. Fedrigo, R. Monot, J. Buttet and W. Harbich, *Surf. Sci.*, 2002, **512**, 201-220.
- 4 W. Moritz, B. Wang, M. L. Bocquet, T. Brugger, T. Greber, J. Wintterlin and S. Günther, *Phys. Rev. Lett.*, 2010, **104**, 136102.
- 5 J. Coraux, A. T. N'Diaye, C. Busse and T. Michely, *Nano Lett.*, 2008, **8**, 565-570.

- 6 S. Joshi, D. Ecija, R. Koitz, M. Iannuzzi, A. P. Seitsonen, J. Hutter, H. Sachdev, S. Vijayaraghavan, F. Bischoff, K. Seufert, J. V. Barth and W. Auwärter, *Nano Lett.*, 2012, **12**, 5821-5828.
- 7 C. R. Woods, L. Britnell, A. Eckmann, R. S. Ma, J. C. Lu, H. M. Guo, X. Lin, G. L. Yu, Y. Cao, R. V. Gorbachev, A. V. Kretinin, J. Park, L. A. Ponomarenko, M. I. Katsnelson, Y. N. Gornostyrev, K. Watanabe, T. Taniguchi, C. Casiraghi, H. J. Gao, A. K. Geim and K. S. Novoselov, *Nat. Phys.*, 2014, **10**, 451-456.
- 8 L. Gao, J. R. Guest and N. P. Guisinger, *Nano Lett.*, 2010, **10**, 3512-3516.
- 9 J. P. Rabe and S. Buchholz, *Science*, 1991, **253**, 424-427.
- 10 F. Silly, *Nanotechnology*, 2012, **23**, 225603.
- 11 L. K. Thomas, A. Kühnle, S. Rode, U. Beginn and M. Reichling, *J. Phys. Chem. C*, 2010, **114**, 18919-18924.
- 12 K. G. Nath, O. Ivasenko, J. M. MacLeod, J. A. Miwa, J. D. Wuest, A. Nanci, D. F. Perepichka and F. Rosei, *J. Phys. Chem. C*, 2007, **111**, 16996-17007.
- 13 M. Kuwabara, D. R. Clarke and D. A. Smith, *Appl Phys Lett*, 1990, **56**, 2396-2398.
- 14 P. Bak, *Rep. Prog. Phys.*, 1982, **45**, 587-629.
- 15 S. De Feyter and F. C. De Schryver, *Chem. Soc. Rev.*, 2003, **32**, 139-150.
- 16 S. De Feyter and F. C. De Schryver, *J. Phys. Chem. B*, 2005, **109**, 4290-4302.
- 17 M. Lackinger and W. M. Heckl, *Langmuir*, 2009, **25**, 11307-11321.
- 18 K. S. Mali, J. Adisojojoso, E. Ghijsens, I. De Cat and S. De Feyter, *Accounts Chem. Res.*, 2012, **45**, 1309-1320.
- 19 A. Stabel, R. Heinz, J. P. Rabe, G. Wegner, F. C. Deschryver, D. Corens, W. Dehaen and C. Siiling, *J. Phys. Chem.*, 1995, **99**, 8690-8697.
- 20 N. T. N. Ha, T. G. Gopakumar, R. Gutzler, M. Lackinger, H. Tang and M. Hietschold, *J. Phys. Chem. C*, 2010, **114**, 3531-3536.
- 21 Y. C. Ye, W. Sun, Y. F. Wang, X. Shao, X. G. Xu, F. Cheng, J. L. Li and K. Wu, *J. Phys. Chem. C*, 2007, **111**, 10138-10141.
- 22 S. Griessl, M. Lackinger, M. Edelwirth, M. Hietschold and W. M. Heckl, *Single Mol.*, 2002, **3**, 25-31.
- 23 Y. Ishikawa, A. Ohira, M. Sakata, C. Hirayama and M. Kunitake, *Chem. Commun.*, 2002, 2652-2653.
- 24 G. J. Su, H. M. Zhang, L. J. Wan, C. L. Bai and T. Wandlowski, *J. Phys. Chem. B*, 2004, **108**, 1931-1937.
- 25 J. M. MacLeod, J. A. Lipton-Duffin, D. Cui, S. De Feyter and F. Rosei, *Langmuir*, 2015, **31**, 7016-7024.
- 26 V. Iancu, K. F. Braun, K. Schouteden and C. Van Haesendonck, *Langmuir*, 2013, **29**, 11593-11599.
- 27 M. S. Babilolai and L. Diekhöner, *Phys. Chem. Chem. Phys.*, 2014, **16**, 11265-11269.
- 28 M. Lackinger, S. Griessl, W. M. Heckl, M. Hietschold and G. W. Flynn, *Langmuir*, 2005, **21**, 4984-4988.
- 29 P. Gilli, V. Bertolasi, V. Ferretti and G. Gilli, *J. Am. Chem. Soc.*, 1994, **116**, 909-915.

- 30 G. Eder, S. Kloft, N. Martsinovich, K. Mahata, M. Schmittl, W. M. Heckl and M. Lackinger, *Langmuir*, 2011, **27**, 13563–13571.
- 31 S. J. H. Griessl, M. Lackinger, F. Jamitzky, T. Markert, M. Hietschold and W. M. Heckl, *Langmuir*, 2004, **20**, 9403-9407.
- 32 M. Li, K. Deng, Y. L. Yang, Q. D. Zeng, M. He and C. Wang, *Phys Rev B*, 2007, **76**, 155438.
- 33 S. Conti and M. Cecchini, *Phys. Chem. Chem. Phys.*, 2016, **18**, 31480-31493.
- 34 J. F. Dienstmaier, K. Mahata, H. Walch, W. M. Heckl, M. Schmittl and M. Lackinger, *Langmuir*, 2010, **26**, 10708-10716.
- 35 E. Loginova, S. Nie, K. Thurmer, N. C. Bartelt and K. F. McCarty, *Phys Rev B*, 2009, **80**, 085430.
- 36 B. Wang, M. Caffio, C. Bromley, H. Fruchtl and R. Schaub, *ACS Nano*, 2010, **4**, 5773-5782.
- 37 P. Zeller and S. Günther, *New J Phys*, 2014, **16**, 083028.
- 38 J. Hutter, M. Iannuzzi, F. Schiffmann and J. VandeVondele, *Wiley Interdiscip. Rev.-Comput. Mol. Sci.*, 2014, **4**, 15-25.
- 39 J. P. Perdew, K. Burke and M. Ernzerhof, *Phys. Rev. Lett.*, 1996, **77**, 3865-3868.
- 40 S. Grimme, *J. Comput. Chem.*, 2006, **27**, 1787-1799.
- 41 M. Lackinger, S. Griessl, L. Kampschulte, F. Jamitzky and W. M. Heckl, *Small*, 2005, **1**, 532-539.
- 42 F. Shayeganfar and A. Rochefort, *Langmuir*, 2014, **30**, 9707-9716.
- 43 A. Tkatchenko, *Phys Rev B*, 2007, **75**, 235411.
- 44